Biomechanics and Modeling in Mechanobiology (2020) 19:2683–2692
https://doi.org/10.1007/s10237-020-01331-6

SHORT COMMUNICATION

Force-dependent recruitment from myosin OFF-state increases end-systolic pressure–volume relationship in left ventricle

Charles K. Mann[1] · Lik Chuan Lee[2] · Kenneth S. Campbell[3] · Jonathan F. Wenk[1,4]

Received: 14 November 2019 / Accepted: 16 April 2020 / Published online: 28 April 2020
© Springer-Verlag GmbH Germany, part of Springer Nature 2020

Abstract
Finite element (FE) modeling is becoming increasingly prevalent in the world of cardiac mechanics; however, many existing FE models are phenomenological and thus do not capture cellular-level mechanics. This work implements a cellular-level contraction scheme into an existing nonlinear FE code to model ventricular contraction. Specifically, this contraction model incorporates three myosin states: OFF-, ON-, and an attached force-generating state. It has been speculated that force-dependent transitions from the OFF- to ON-state may contribute to length-dependent activation at the cellular level. The current work investigates the contribution of force-dependent recruitment out of the OFF-state to ventricular-level function, specifically the Frank–Starling relationship, as seen through the end-systolic pressure–volume relationship (ESPVR). Five FE models were constructed using geometries of rat left ventricles obtained via cardiac magnetic resonance imaging. FE simulations were conducted to optimize parameters for the cellular contraction model such that the differences between FE predicted ventricular pressures for the models and experimentally measured pressures were minimized. The models were further validated by comparing FE predicted end-systolic strain to experimentally measured strain. Simulations mimicking vena cava occlusion generated descending pressure volume loops from which ESPVRs were calculated. In simulations with the inclusion of the OFF-state, using a force-dependent transition to the ON-state, the ESPVR calculated was steeper than in simulations excluding the OFF-state. Furthermore, the ESPVR was also steeper when compared to models that included the OFF-state without a force-dependent transition. This suggests that the force-dependent recruitment of thick filament heads from the OFF-state at the cellular level contributes to the Frank–Starling relationship observed at the organ level.

Keywords Finite element · Three-state model · Contraction · Multi-scale model

1 Introduction

Cardiovascular disease (CVD) is prevalent in many adults, with greater than one in three American adults having at least one type of CVD, which accounts for a significant fraction of deaths (Benjamin et al. 2019). While the 5-year survival rate after a heart failure diagnosis improved until the year 2000, it has plateaued and has remained around 50% (Benjamin et al. 2019), which could indicate that the effectiveness of recent research and treatment techniques is also reaching a plateau. Finite element (FE) modeling has been used increasingly for cardiac research, typically for simulations of the left ventricle (LV) during the cardiac cycle (Guccione and McCulloch 1993; Guccione et al. 1993). Some of these models are phenomenological and are able to show reasonable agreement between FE predicted strains and experimental data (Guccione et al. 1993; Hunter et al. 1998), while others incorporate cellular-level contraction models (Campbell 2014; Rice et al. 2008) into LV models to reproduce organ-level phenomena such as pressure–volume loops (PV loops) and linear end-systolic pressure–volume relationships (ESPVR) (Shavik et al. 2017; Zhang et al. 2018). These well-known organ-level phenomena, specifically ESPVR, are used in research settings as a measure of contractility. Efforts have been made to find ways

✉ Jonathan F. Wenk
jonathan.wenk@uky.edu

[1] Department of Mechanical Engineering, University of Kentucky, 269 Ralph G. Anderson Building, Lexington, KY 40506-0503, USA

[2] Department of Mechanical Engineering, Michigan State University, East Lansing, MI, USA

[3] Division of Cardiovascular Medicine, Department of Physiology, University of Kentucky, Lexington, KY, USA

[4] Department of Surgery, University of Kentucky, Lexington, KY, USA

to use ESPVR or estimations of it in the clinic (Burkhoff et al. 2005; Shoucri and Kohar 2012). Thus, models that incorporate physiological mechanisms to predict clinically relevant characteristics may better translate to patient care.

There are multiple models of myocyte contraction (Trayanova and Rice 2011) that have expanded upon the Huxley two-state model (Huxley 1957). These various models have been shown to capture certain experimentally observed properties of myocytes such as thick and thin filament cooperativity, force–velocity relationships, and tension recovery (Campbell 2014; Rice et al. 2008; Schneider et al. 2006). Length-dependent activation in muscles is well documented experimentally, but the underlying mechanisms remain unclear. One of the latest hypotheses is that structural re-arrangement of thick filaments contributes to the effect. Specifically, length-dependent activation reflects recruitment of myosin heads from an OFF-state (which cannot interact with actin) to an ON-state (which can interact with actin) (Ait-Mou et al. 2016; Kampourakis et al. 2016). This hypothesis is supported by simulations which reproduce length-dependent activation measured in isolated myocardium when the rate of the OFF to ON transition increases linearly with force (Campbell et al. 2018). The current study implements the three-state contraction model (myosin OFF-state, myosin ON-state, and myosin force-generating state) from that work into an existing nonlinear 3D FE code to model healthy Sprague–Dawley rat LVs. As the force-dependent transition relies on both passive and active stress within the sarcomere, the passive response of the tissue is decomposed into that of the myofiber and the remaining bulk material (i.e., collagen, elastin, gel-like cells, interstitial fluid, etc.). It is shown that the model predictions are in good agreement with experimental measurements and that length-dependent activation is captured both at the cellular level and organ level, as seen in physiologically realistic force–pCa curves and ESPVR values calculated from simulations. Furthermore, it is shown that when the FE models are optimized using a previously developed two-state cellular contraction model ("two-state model") where the myosin OFF-state is omitted (Zhang et al. 2018), the ESPVR values calculated are less than those calculated from the three-state implementation, suggesting that transitions to and from the myosin OFF-state contribute to the Frank–Starling mechanism seen at the organ level. This method was validated using the animal-specific FE models, which were fit to experimentally measured LV pressures and then compared to experimentally measured end-systolic strain.

2 Materials and methods

2.1 Experimental measurements

Details of the experiments have been published (Zhang et al. 2017). Briefly, 3D displacement encoding with stimulated echoes cardiovascular magnetic resonance (DENSE CMR) imaging was conducted (7T Bruker ClinScan system, Bruker, Ettlingen, Germany) on five female Sprague–Dawley rats. These images were used to create contours of the LV wall for FE mesh generation, and then, calculations were performed using DENSE analysis (Spottiswoode et al. 2007) to assess end-systolic strains. This was followed by LV pressure measurements using a pressure transducer (SPR-903, Millar Instruments, Houston, TX, USA). All animal procedures were approved by the Institutional Animal Care and Use Committee at the University of Kentucky and were in agreement with the guidelines by the National Institutes of Health for the care and use of laboratory animals (NIH Publication 85–23, revised 1996). All values are reported as mean ± standard deviation.

2.2 Finite element modeling

For each of the animals, an LV FE model was created based on geometric surfaces generated from the CMR data. The reference configuration of the LV was defined to be at early diastole. The mesh was created using 8-node hexahedral brick elements, and the myocardium was split into three layers: epicardium, mid-myocardium, and endocardium (Fig. 1) (Zhang et al. 2015). Each layer was assigned unique reference sarcomere lengths of 1910 nm, 1850 nm, and 1780 nm from epicardium to endocardium, respectively (Guccione et al. 1993). Helical fiber angles were also assigned to each layer as $-60°$, $0°$, and $+60°$, relative to the circumferential direction, in the epicardium, mid-myocardium, and endocardium, respectively. This fiber angle is used to create an orthogonal local coordinate system within each element (Fig. 1). This local coordinate system consists of the fiber direction, sheet direction, and sheet normal direction. It should be noted that in the current study, the sheet angle was set to $0°$. Finally, endocardial contours were drawn at multiple time points on each CMR image during the filling phase and ejection phase. These contour data were then used to estimate the LV cavity volume as a function of time during the entire cardiac cycle and were implemented in the simulation as a boundary condition specifying the volumetric flow rate (dV/dt) into and out of the LV. The passive and active material models, discussed in detail below, were both implemented in a user-defined material subroutine within the explicit nonlinear FE solver LS-DYNA (Livermore Software Technology Corporation, Livermore, CA, USA).

Each simulation was performed for the time course of one cardiac cycle, after being loaded to end-diastole from the reference configuration. Ventricular volume was calculated at each time step from the specified flow rate boundary condition (Fig. 2). Additionally, an intracellular calcium transient was specified, which was adapted from experimental measurements (Laurita and Singal 2001) and independent

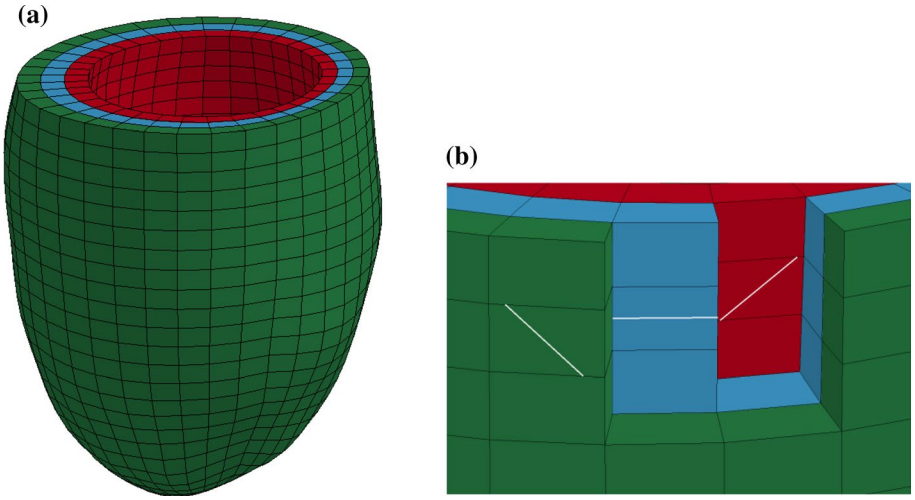

Fig. 1 **a** Representative LV FE mesh (TrueGrid; XYZ Scientific, Inc., Livermore, CA, USA). The ventricle is partitioned into three parts transmurally: epicardium (green), mid-myocardium (blue), and endocardium (red). **b** Assigned fiber angles shown for representative elements as white lines, giving −60°, 0°, and +60° orientations in the epicardium, mid-myocardium, and endocardium

of the cross-bridge kinetics (Fig. 2). The peak value of calcium was based on Campbell et al. (2018). At each time step, the change in cavity volume causes the wall to deform, which induces stretch along the myofiber direction, and thus changes the sarcomere length. This change in sarcomere length, along with the passive stress in the myofiber and calcium concentration ($[Ca^{2+}]$), is used by the cellular contraction model to calculate active stress produced by a sarcomere. This active stress is then scaled up proportionally by the density of myosin heads in a cardiac sarcomere. The total stress state in the LV wall, which is the sum of the passive and active stress, is then balanced by the calculated intraventricular pressure.

2.3 Active contraction model

The cellular-level model formulation was previously presented in Campbell et al. (2018). In the current work, the three-state cellular-level contraction model is implemented as an explicit set of ODEs in our FE framework. The scheme consists of two states for the thin filaments, and three states that the thick filaments can transition between. Thin filament states will be denoted as N_{OFF} and N_{ON}, with a subset of the N_{ON} population (N_{BOUND}) bound to thick filaments to form cross-bridges. The three thick filament states can be described as (1) OFF, (2) ON and detached, or (3) ON, bound, and force generating (Fig. 3). The thick filament

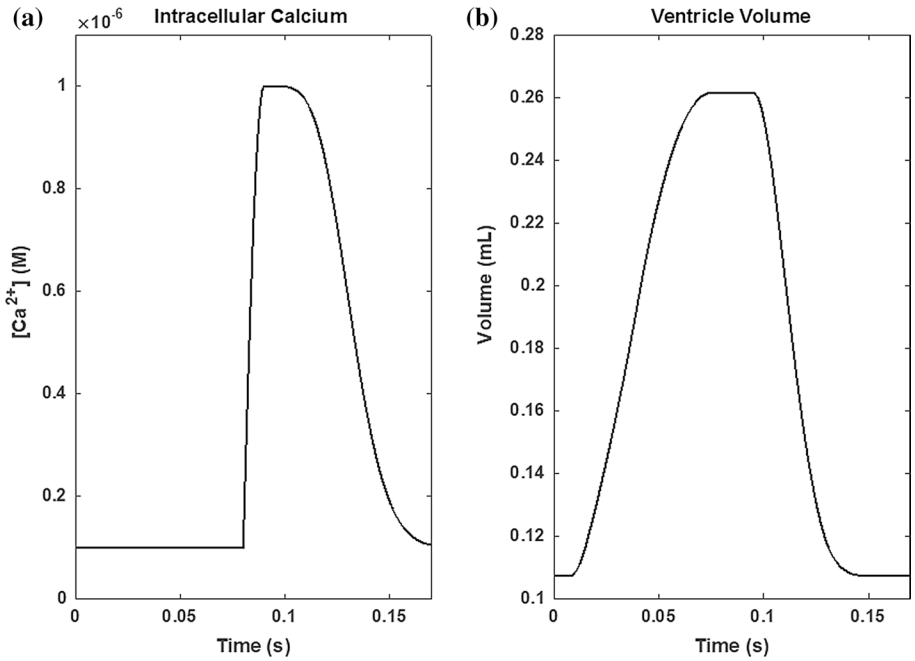

Fig. 2 Representative intracellular calcium transient (**a**) and ventricular volume (**b**) used to drive LV FE model simulations

states will be represented as M_{OFF}, M_{ON}, and $M_{FG}(x)$. Some underlying assumptions of this model are:

(1) Myosin heads can only bind to sites on actin from the M_{ON} state at a location x, where $x=0$ represents a binding site directly opposite the myosin head (Fig. 3). This x domain is discretized into n intervals, thus discretizing the M_{FG} state into n populations, ranging from -10 to 10 nm. The total force-generating cross-bridge population is therefore $\sum_{i=1}^{n} M_{FG,x_i}$. In this study, n is set to 21, as further refinement does not affect the solution and increases computation time. Conversely, less refinement can lead to the strain-dependent cross-bridge mechanics being neglected during systole.
(2) Binding sites that are activated cannot become inactive while thick filaments are bound to them, i.e., there is no direct transition from the N_{BOUND} state to the N_{OFF} state.
(3) In the reference configuration, all thick filaments are in the M_{OFF} state, and all thin filaments are in the N_{OFF} state.

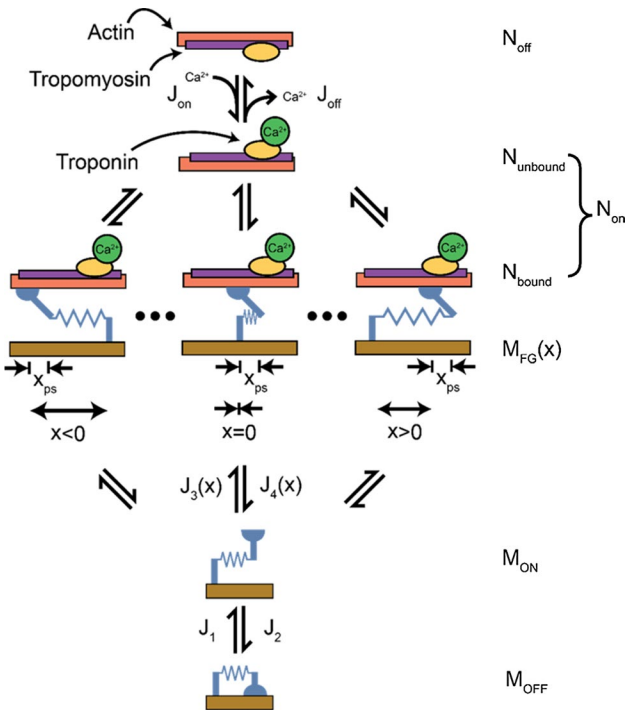

Fig. 3 Schematic of cellular-level three-state contraction scheme. Myosin heads are represented in blue, actin filaments are represented in pink. From the top, binding sites on the actin filament can transition between an OFF- and ON-state through the transitions J_{on} and J_{off} which are calcium regulated. Myosin heads transition between the OFF- and ON-state via J_1 (force dependent) and J_2. Finally, myosin heads in the ON-state can attach to the force-generating state $M_{FG}(x)$ via $J_3(x)$ and detach via $J_4(x)$. Representative cross-bridges for a negative, neutral, and positive attachment are shown in the center of the figure

The proportion of potential binding sites for cross-bridges at each time step is dependent on the overlap ($N_{OVERLAP}$) between the thick and thin filaments which relies on sarcomere length.

$$N_{OVERLAP} = \begin{cases} 0 & \text{if } l_{overlap} \le 0 \\ \frac{l_{overlap}}{l_{maxoverlap}} & \text{if } 0 < l_{overlap} < l_{maxoverlap} \\ 1 & \text{if } l_{maxoverlap} \le l_{overlap} \end{cases}$$

where

$$l_{overlap} = l_{thin} + l_{thick} - l_{sarcomere}$$
$$l_{maxoverlap} = l_{thick} - l_{bare}$$

l_{thin}, l_{thick}, $l_{sarcomere}$, and l_{bare} are the lengths of the thin filament, thick filament, sarcomere, and thick filament bare zone, respectively. In the case that $l_{sarcomere} < l_{thin}$, then

$$N_{overlap} = 1 - l_{falloff}\left(l_{thin} - l_{sarcomere}\right)$$

where $l_{falloff}$ is a parameter describing the fraction of binding sites that are removed from the overlap in the model.

The thin filament transitions are given by

$$\frac{dN_{OFF}}{dt} = -J_{ON} + J_{OFF}$$
$$\frac{dN_{ON}}{dt} = -J_{OFF} + J_{ON}$$

where J_{ON} and J_{OFF} are the fluxes through the ON- and OFF-states, respectively, defined as

$$J_{ON} = k_{ON}\left[Ca^{2+}\right]\left(N_{OVERLAP} - N_{ON}\right)\left(1 + k_{COOP}\left(\frac{N_{ON}}{N_{OVERLAP}}\right)\right)$$
$$J_{OFF} = k_{OFF}\left(N_{ON} - N_{BOUND}\right)\left(1 + k_{COOP}\left(\frac{N_{OVERLAP} - N_{ON}}{N_{OVERLAP}}\right)\right)$$

and k_{ON}, k_{OFF}, and k_{COOP} are rate constants. In the event that $N_{OVERLAP} \le N_{ON}$, the $\left(N_{OVERLAP} - N_{ON}\right)$ term is zeroed so that no more binding sites on the thin filaments can activate, and there is no cooperative detachment effect from off binding sites.

The thick filament transitions are given by

$$\frac{dM_{OFF}}{dt} = -J_1 + J_2$$
$$\frac{dM_{ON}}{dt} = \left(J_1 + \sum_{i=1}^{21} J_{4,x_i}\right) - \left(J_2 + \sum_{i=1}^{21} J_{3,x_i}\right)$$
$$\frac{dM_{FG,i}}{dt} = J_{3,x_i} - J_{4,x_i}$$

where J_1–J_4 are the fluxes through the states, defined as

$$J_1 = k_1\left(1 + k_{\text{FORCE}}\left(F_{\text{P,fiber}} + F_{\text{Active}}\right)\right)M_{\text{OFF}}$$
$$J_2 = k_2 M_{\text{ON}}$$
$$J_{3,x_i} = k_3 e^{\frac{-k_{\text{cb}}x_i^2}{2k_{\text{B}}T}} M_{\text{ON}}\left(N_{\text{ON}} - N_{\text{BOUND}}\right)$$
$$J_{4,x_i} = \left(k_{4,0} + k_{4,1}x_i^4\right)M_{\text{FG},x_i}$$

Note that J_1 includes both active (F_{Active}) and passive ($F_{\text{P,fiber}}$) stress; thus, a non-activated, stretched sarcomere will more quickly recruit myosin heads from the super-relaxed OFF-state. Note also that the thick and thin filament populations are coupled due to the inclusion of the (N_{ON}–N_{BOUND}) term in the flux through the M_{ON} state. Further detail can be found in Campbell et al. (2018). This creates a system of ordinary differential equations to be solved simultaneously. In this implementation, the system is solved using a fourth-order Runge–Kutta method with a time step of 1 μs, which is used as the time step in the FE simulation of the cardiac cycle.

Once the populations are solved for, they are shifted by linear interpolation to account for interfilamentary movement so that for a change of Δx in one half of the sarcomere, the entire M_{FG} population experiences a shift of $(1/2)\Delta x$ to become M^*_{FG} (Campbell 2014; Huxley et al. 1994; Tajima et al. 1994). The stress generated by a sarcomere, along the myofiber direction, can then be calculated from the shifted populations by

$$F_{\text{active}} = N_0 k_{\text{cb}} \sum_{i=1}^{21} M^*_{\text{FG},x_i}\left(x_i + x_{\text{ps}}\right)$$

N_0 is the density of myosin heads (assumed to be 6.9×10^{16} m^{-2}) and k_{cb} is the spring stiffness of a cross-bridge. Once calculated, 25% of the magnitude of the active stress generated is added to the sheet and sheet normal directions to account for muscle fiber branching and the transmission of force via connective tissue (Zhang et al. 2018).

2.4 Passive material response

Due to the force-reliant nature of the transition of thick filament heads out of the OFF-state, it was necessary to additively decompose the passive model into two parts: the myofiber passive model and the response of the remaining bulk material. This moves the passive material model closer to a structural model. The bulk material of the LV was assumed to be nearly incompressible with a bulk modulus of $\kappa = 2.0\times10^6$ kPa, transversely isotropic, and hyperelastic. As such, the passive stresses are derived from the following strain energy function:

$$W_{\text{B}} = \frac{C}{2}\left(e^{\left(b_f E_{11}^2 + b_t\left(E_{22}^2+E_{33}^2+E_{23}^2+E_{32}^2\right)+b_{fs}\left(E_{12}^2+E_{21}^2+E_{13}^2+E_{31}^2\right)-1\right)}\right) + \frac{\kappa^2}{2}(J-1)^2$$

where E_{11} is the strain in the fiber direction, E_{22} is the strain in the sheet direction, E_{33} is the strain in the sheet normal direction, and the remaining terms are shear strains (Guccione et al. 1993), while J is the Jacobian determinant of the deformation gradient. Values for the material constants b_f, b_t, and b_{fs} were chosen as 18.48, 3.58, and 1.627, respectively (Guccione et al. 2001; Zhang et al. 2015).

The myofiber passive stresses ($F_{\text{P,fiber}}$) are derived from the following strain energy function:

$$W_{\text{fiber}} = \begin{cases} C_2\left[e^{C_3(\alpha-1)^2} - 1\right] & \alpha > 1 \\ 0 & \alpha \le 1 \end{cases}$$

where C_2 and C_3 are material constants, and α is the stretch along the myofiber direction (Xi et al. 2019). This gives a nonlinear stress response in tension, but does not allow the myofiber to bear any compressive load. The parameters C, C_2 and C_3 were chosen such that the end-diastolic pressure from the models matched experimentally measured end-diastolic pressures and such that the bulk material stress was approximately twice that of the myofibers at end-diastole (Xi et al. 2019). Values chosen were $C = 0.266 \pm 0.087$ kPa, $C_2 = 0.172 \pm 0.063$ kPa, and $C_3 = 7.6 \pm 4$.

2.5 Model optimization and validation

Parameters for the embedded cellular contraction model were numerically optimized using LS-OPT (Livermore Software Technology Corporation, Livermore, CA) to minimize the difference between FE predicted ventricular pressures and experimentally obtained pressures. A hybrid approach using a combination of simulated annealing and the sequential response surface method was used as previously described (Zhang et al. 2018). Seven parameters were optimized, and pressures were compared at a minimum of seven time points during systole and relaxation. Ranges for these parameters were chosen to keep the transition rates within physiologically reasonable magnitudes. The parameters involved in the optimization are shown in Table 1.

Further validation of the models included comparing mid-ventricular end-systolic strains predicted by the models to experimentally measured strains from DENSE CMR. In order to provide multi-scaled validation, simulations were conducted using the final optimized parameters in single-element FE models to mimic single-cell experiments from the literature. These simulations included a cell developing maximum tension at saturating calcium, the generation of force–pCa curves to investigate length-dependent shifting of pCa_{50} values, and tension recovery simulations (ktr). Finally, vena cava occlusion was simulated in the LV FE models in order to generate a series of descending PV loops (Fig. 4) from which the ESPVR was calculated. In order to simulate

Table 1 Parameter values for the three-state cellular contraction model for all five models

	Case 1	Case 2	Case 3	Case 4	Case 5
a_on (M^{-1} s^{-1})	5.0e7	5.0e7	5.8e7	5.0e7	8.0e7
a_off (s^{-1})	90.00	70.00	95.00	76.01	115.01
k_1 (s^{-1})	6.02	7.70	8.00	9.15	6.50
k_2 (s^{-1})	61.18	92.88	96.01	150.00	95.01
$k_{4,0}$ (s^{-1})	615.49	900.00	490.82	510.74	381.41
$k_{4,1}$ (nm^{-4})	1.84	2.00	8.66	14.33	16.78
k_coop (no units)	5.00	4.02	4.00	4.00	4.00
x_ps[a] (nm)	5	5	5	5	5
k_force[a] (N^{-1} m^{-2})	8e−5	8e−5	8e−5	8e−5	8e−5
k_3^a (nm^{-1} s^{-1})	1000	1000	1000	1000	1000

[a]Values that were set and not varied as part of the optimization

a vena cava occlusion, the end-diastolic volume (EDV) was gradually reduced over a series of FE simulations. This was accomplished by scaling the volumetric flow rate that was used as a boundary condition to drive the simulation. Based on previous studies, the flow rate into the ventricle was reduced, while the flow rate out of the LV was adjusted to conserve the ejection fraction (Olah et al. 2015; Konstam and Abboud 2017). This shifts each PV loop down and to the left. In the current study, the end-diastolic volume was gradually reduced by 30%. This process was repeated in the LV model using a previous cellular contraction model that omitted the myosin OFF-state, i.e., the two-state model (Zhang et al. 2018).

3 Results

3.1 Organ-level function

All five of the animal-specific FE models showed good agreement with the experimentally measured pressure values during the optimization procedure. An example of this is shown in Fig. 4. The overall fit to the pressure points during ejection and relaxation was within ± 5%, and the final optimized parameters are listed in Table 1. As noted before, each model was fit to the end-diastolic pressure and volume, so that the passive parameters C, C_2, and C_3 could be defined before the optimization. In order to further validate the models and compare their performance to the previous two-state implementation (Zhang et al. 2018), mid-ventricular end-systolic strain was calculated. Both the three-state and two-state models showed good agreement with 5 of the 6 CMR measured end-systolic strain components, i.e., no statistically significant difference was found (Table 2). With respect to the longitudinal strain, both implementations showed a statistically significant difference from the CMR strain (-0.159 ± 0.010 vs. -0.106 ± 0.011 [CMR vs. 3-state] and -0.159 ± 0.010 vs. -0.085 ± 0.008 [CMR vs. 2-state], both $^*p < 0.05$). However, the three-state model is also significantly different from the two-state model (-0.106 ± 0.011 vs. -0.085 ± 0.008, $^\dagger p < 0.05$) and is closer to the CMR measured value.

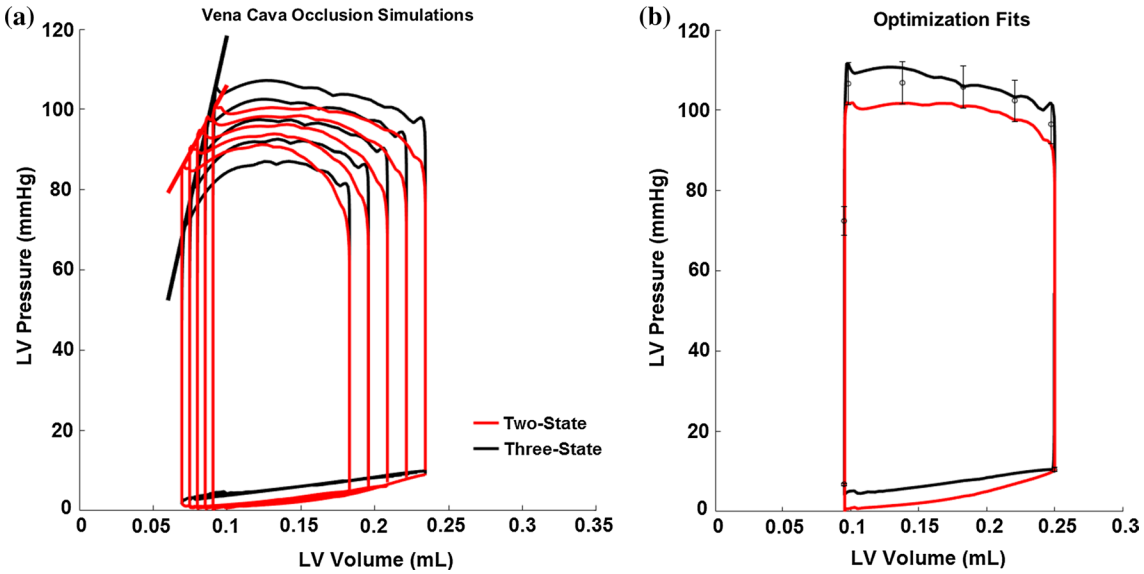

Fig. 4 **a** Representative pressure–volume loops generated from simulating vena cava occlusion. The diagonal lines that are fitted to end-systole represent the end-systolic pressure volume relationship (ESPVR). **b** Pressure–volume loops that were generated during the optimization of the two-state and three-state models to the experimental data. Note that the circular markers indicate experimentally measured values with range bars that represent ± 5%

The simulated vena cava occlusion was conducted for each animal-specific LV FE model, using both the three-state and two-state contraction models. A representative set of PV loops, along with ESPVR slopes, are shown in Fig. 4. The three-state ESPVR value with a force-dependent transition to the ON-state is significantly higher than the two-state model, where the OFF-state is omitted ($p < 0.05$) (Fig. 5). The average ESPVR from the three-state model was found to be 1380.89 ± 89.62 mmHg mL^{-1} and for the two-state model was 764.47 ± 148.01 mmHg mL^{-1}, which both fall near or within the physiologically realistic bounds of 1000–7000 mmHg mL^{-1} (Pacher et al. 2008).

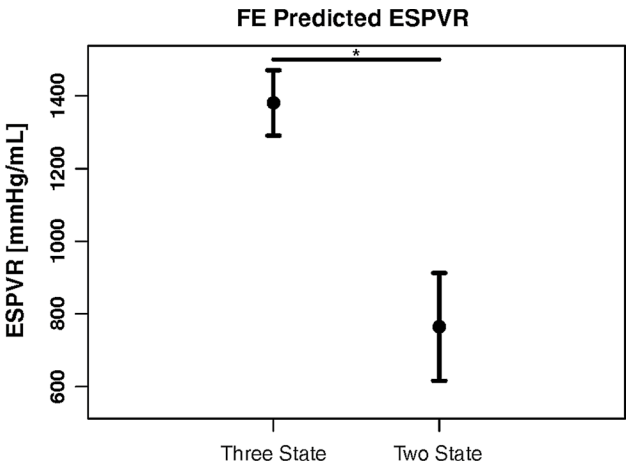

Fig. 5 Calculated ESPVR values for the three-state contraction model as compared to a two-state contraction model that omits the myosin OFF-state; $n = 5$. *$p < 0.05$, unpaired Student's t tests assuming equal variances

3.2 Cellular-level function

The results of the single-element FE simulations for a sarcomere length of 2300 nm, which used the optimized parameters from each of the animal-specific cases, are shown in Table 3. The maximum tension generated was found to be 212 ± 5.32 kPa. The pCa_{50} value at 2300 nm was found to be $6.34 \pm .02$, which is higher than when the sarcomere length is 1900 nm at $6.28 \pm .03$. This shows a leftward shift in the force–pCa curve, which is consistent with length-dependent activation at the cellular level (Mamidi et al. 2014; Marcucci et al. 2017) (Fig. 6). Also, the hill coefficients (n_H) showed a decreasing trend at longer sarcomere lengths, consistent with previous reports (Pulcastro et al. 2016). For a sarcomere length of 1900 nm, $n_H = 4.02 \pm 0.08$, but for 2300 nm, $n_H = 3.31 \pm 0.07$. Finally, the ktr values are consistent with extrapolated values from the literature (de Tombe and Stienen 2007), i.e., previous experiments report values at temperatures increasing from 15 to 25 °C. The current results ($ktr_{max} = 77.07 \pm 4.89$ s^{-1} and $ktr_{min} = 18.58 \pm 5.45$ s^{-1}) are meant to represent in vivo function, where the temperature would be 37 °C.

4 Discussion

Frank–Starling is an important mechanism for beat-to-beat regulation of contraction in the heart. Length-dependent activation (LDA) at the cellular level is an important underlying mechanism for this, and work has shown that passive force and mechanosensitive transitions in the thick filament may be responsible for LDA (Ait-Mou et al. 2016; Fukuda et al. 2001). The current model incorporates a novel three-state contraction scheme, which includes a myosin OFF-state and a force-modulated transition out of this state, into an organ-level FE model. This model is able to reproduce experimentally measured pressure and wall deformation during the cardiac cycle. Thus, the framework can make predictions regarding organ-level function by considering cell-level mechanisms, traversing the scale between sarcomeric function and ventricular function.

This three-state contraction model, while not capturing all of the biochemical pathways of cross-bridge cycling, is able to incorporate many important aspects of muscle

Table 2 End-systolic strain components averaged at the mid-LV in the mid-myocardial layer

	E_{cc}	E_{rr}	E_{ll}	E_{cr}	E_{cl}	E_{rl}
CMR	-0.200 ± 0.022	0.553 ± 0.075	-0.159 ± 0.010	0.068 ± 0.013	0.055 ± 0.012	0.085 ± 0.017
3 state	-0.189 ± 0.011	0.522 ± 0.061	-0.106 ± 0.011*†	0.056 ± 0.010	0.062 ± 0.014	0.087 ± 0.012
2 state	-0.185 ± 0.010	0.510 ± 0.056	-0.085 ± 0.008*	0.058 ± 0.014	0.064 ± 0.011	0.091 ± 0.013

Data are mean ± standard deviation; $n = 5$. Multiple comparisons between groups (i.e., experimental CMR, three-state model, two-state model) were performed using one-way ANOVA with post hoc Bonferroni t tests

*$p < 0.05$ for comparisons between model-predicted and experimentally measured strains

$^{\dagger}p < 0.05$ for comparisons between three-state model and two-state model

contraction including interfilamentary movement, the cooperative nature of thick and thin filament binding, and strain dependence of cross-bridge kinetics. Compared to the previously embedded two-state model, the current model has fewer parameters that required optimization during the fitting procedure (Zhang et al. 2018). This decreased the time needed to run a numerical optimization while still utilizing a more intricate contraction scheme. This is advantageous for future translation of this technique to clinical data.

The current approach is able to reproduce LDA in a physiologically realistic way, shown at the cellular level as a leftward shift in the force–pCa curve (Fig. 6). Additionally, the maximum isometric contraction that is generated at the cellular level was higher with the three-state model. As reported previously (Zhang et al. 2018), the maximum contractile stress generated by the two-state model was 135.3 ± 5.2 kPa. In the current work, the maximum contractile stress generated by the three-state model was 212.1 ± 11.9 kPa. Considering that both models generate zero stress when the sarcomere length is reduced to the slack length, it can be inferred that the slope of the stress–length relation is steeper for the three-state model. That is, for the same sarcomere length and level of calcium, the presence of force-dependent recruitment leads to higher contractility. Both the force–pCa and stress–length relations suggest that force-dependent recruitment from the OFF-state at the cell level produces a steeper ESPVR at the organ level.

In order to confirm that these results are caused by force-dependent recruitment, and not just the presence of the OFF-state, PV loops were generated with the *k*_force parameter set to zero and the *k*_1 parameter increased. When this was done, the ESPVR dropped to a value in line with the two-state model. This implies that force-dependent recruitment is a critical factor in ESPVR. As the sarcomere is passively stretched, myosin heads are recruited into the myosin ON-state, which during contraction increases the overall number of force-generating cross-bridges leading to a higher active stress (Table 3). In the two-state contraction model, all myosin already exists in the myosin ON-state, restricting the length dependence of the number of cross-bridges to the overlap of the thick and thin filaments. It should be noted that in our previous work, the two-state model was compared to a phenomenological contraction model (time-varying elastance) (Zhang et al. 2018). It was found that the phenomenological model was unable to reproduce the experimentally measured pressure profiles and thus did not converge during the optimization. In addition to this deficiency, phenomenological models are unable to represent the presence of the OFF-state, which has been shown to play a role in the development of heart disease (Kampourakis et al. 2018). Thus, these models may not be able to capture the effects of this cellular mechanism on organ-level function.

A further improvement to the current model is the advancement of the passive material constitutive law. Previously, the entire passive response of the cardiac tissue in the FE model was represented by the bulk tissue (Zhang et al. 2018). However, during contraction, much of the tissue response is compression and myofibers cannot bear a compressive load. This affected the force-dependent recruitment of myosin, especially during the latter half of systole as the magnitude of compression increases. This motivated the decomposition of the passive response discussed above, which resolved this issue and advanced the model more toward a structural model rather than phenomenological.

Finally, it was shown that this three-state implementation is able to predict mid-ventricular end-systolic strains reasonably well when compared to experimentally obtained strains. While the longitudinal strain component from the three-state

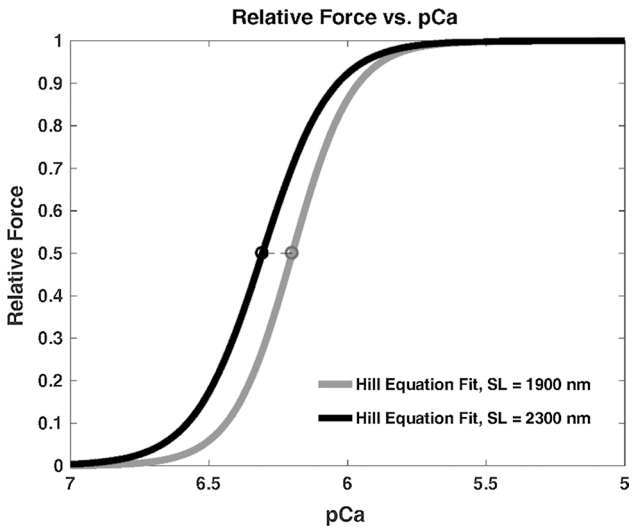

Fig. 6 Representative single-element FE predicted force at varying pCa values showing that as sarcomere length increases, the force versus pCa curve shifts left, which captures the effect of length-dependent activation. The circles indicate the value at pCa_{50}

Table 3 Single-cell FE simulation results for a sarcomere length of 2300 nm using the three-state model

	Case 1	Case 2	Case 3	Case 4	Case 5
T_{max} (kPa)	218.4	193.8	219.3	206.5	222.5
ktr_{max} (s^{-1})	69.70	77.19	83.08	79.16	76.25
ktr_{min} (s^{-1})	17.39	24.44	14.81	23.99	12.29
n_H	3.27	3.39	3.13	3.52	3.25
pCa_{50}	6.32	6.29	6.36	6.31	6.42

T_{max} represents the maximum tension generated by the half-sarcomere at saturated calcium. ktr_{max} and ktr_{min} are the maximum and minimum rates of force recovery, n_H is the Hill coefficient for the fit of the force–pCa curves, and pCa_{50} is the pCa at which the cell generates a tension equal to half of T_{max}

implementation was statistically different than experimental data, it was also statistically different from the two-state implementation and closer to the CMR value. This implies that while not perfect, the predicted strain for this component was improved and trending toward the experimental data.

There are still limitations associated with this model. This includes the lack of bidirectional coupling between the intracellular calcium and the cross-bridge kinetics, as cross-bridge kinetics do not impact the calcium transient. This will be investigated in future studies. While the passive material law has been improved, allowing for a more accurate representation of stress within a myofiber, the law is still not fully structurally based (Xi et al. 2019). This will be addressed in the next iteration of this modeling framework. Finally, future FE models will include the right ventricular geometry and loading in the model.

This work shows how multi-scale modeling can successfully test hypotheses regarding the effects of cellular-level mechanisms on organ-level function, specifically the relationship between the myosin OFF-state and ESPVR. By representing active contraction of the heart in a way that captures realistic cross-bridge distributions, the new approach advances the field toward mechanistic models rather than phenomenological models, displaying greater predictive power without sacrificing fits to experimental data, such as pressure or strain. In addition, recent work has exposed the importance of this force-dependent transition of myosin heads, which is a pathway that is represented in the current three-state model and suggests perturbations to this transition may be important in the development of cardiac hypertrophy (Kampourakis et al. 2018). This is a significant step in advancing the relevance of computational modeling toward its potential of predicting cardiac function in diseased states or with potential interventions (Campbell et al. 2019).

Acknowledgements This study was supported by grants from the National Institutes of Health (U01HL133359 and S10RR029541), as well the Halcomb Fellowship in Medicine and Engineering from the University of Kentucky.

References

Ait-Mou Y, Hsu K, Farman GP, Kumar M, Greaser ML, Irving TC, de Tombe PP (2016) Titin strain contributes to the Frank–Starling law of the heart by structural rearrangements of both thin- and thick-filament proteins. Proc Natl Acad Sci USA 113(8):2306–2311. https://doi.org/10.1073/pnas.1516732113

Benjamin EJ, Muntner P, Alonso A, Bittencourt MS, Callaway CW, Carson AP (2019) Heart disease and stroke statistics-2019 update: a report from the American Heart Association. Circulation 139(10):e56–e528. https://doi.org/10.1161/CIR.0000000000000659

Burkhoff D, Mirsky I, Suga H (2005) Assessment of systolic and diastolic ventricular properties via pressure-volume analysis: a guide for clinical, translational, and basic researchers. Am J Physiol Heart Circ Physiol 289(2):H501–H512. https://doi.org/10.1152/ajpheart.00138.2005

Campbell KS (2014) Dynamic coupling of regulated binding sites and cycling myosin heads in striated muscle. J Gen Physiol 143(3):387–399. https://doi.org/10.1085/jgp.201311078

Campbell KS, Janssen PML, Campbell SG (2018) Force-dependent recruitment from the myosin off state contributes to length-dependent activation. Biophys J 115(3):543–553. https://doi.org/10.1016/j.bpj.2018.07.006

Campbell KS, Yengo CM, Lee LC, Kotter J, Sorrell VL, Guglin M, Wenk JF (2019) Closing the therapeutic loop. Arch Biochem Biophys 663:129–131. https://doi.org/10.1016/j.abb.2019.01.006

de Tombe PP, Stienen GJ (2007) Impact of temperature on cross-bridge cycling kinetics in rat myocardium. J Physiol 584(Pt 2):591–600. https://doi.org/10.1113/jphysiol.2007.138693

Fukuda N, Sasaki D, Ishiwata S, Kurihara S (2001) Length dependence of tension generation in rat skinned cardiac muscle: role of titin in the Frank–Starling mechanism of the heart. Circulation 104(14):1639–1645. https://doi.org/10.1161/hc3901.095898

Guccione JM, McCulloch AD (1993) Mechanics of active contraction in cardiac muscle: part I—constitutive relations for fiber stress that describe deactivation. J Biomech Eng 115(1):72–81

Guccione JM, Waldman LK, McCulloch AD (1993) Mechanics of active contraction in cardiac muscle: part II—cylindrical models of the systolic left ventricle. J Biomech Eng 115(1):82–90

Guccione JM, Moonly SM, Moustakidis P, Costa KD, Moulton MJ, Ratcliffe MB, Pasque MK (2001) Mechanism underlying mechanical dysfunction in the border zone of left ventricular aneurysm: a finite element model study. Ann Thorac Surg 71(2):654–662. https://doi.org/10.1016/s0003-4975(00)02338-9

Hunter PJ, McCulloch AD, ter Keurs HE (1998) Modelling the mechanical properties of cardiac muscle. Prog Biophys Mol Biol 69(2–3):289–331

Huxley AF (1957) Muscle structure and theories of contraction. Prog Biophys Biophys Chem 7:255–318

Huxley HE, Stewart A, Sosa H, Irving T (1994) X-ray diffraction measurements of the extensibility of actin and myosin filaments in contracting muscle. Biophys J 67(6):2411–2421. https://doi.org/10.1016/S0006-3495(94)80728-3

Kampourakis T, Sun YB, Irving M (2016) Myosin light chain phosphorylation enhances contraction of heart muscle via structural changes in both thick and thin filaments. Proc Natl Acad Sci USA 113(21):E3039–E3047. https://doi.org/10.1073/pnas.1602776113

Kampourakis T, Ponnam S, Irving M (2018) Hypertrophic cardiomyopathy mutation R58Q in the myosin regulatory light chain perturbs thick filament-based regulation in cardiac muscle. J Mol Cell Cardiol 117:72–81. https://doi.org/10.1016/j.yjmcc.2018.02.009

Konstam MA, Abboud FM (2017) Ejection fraction: misunderstood and overrated (chaning the paradigm in categorizing heart failure). Circulation 135:717–719. https://doi.org/10.1161/CIRCULATIONAHA.116.025795

Laurita KR, Singal A (2001) Mapping action potentials and calcium transients simultaneously from the intact heart. Am J Physiol Heart Circ Physiol 280(5):H2053–H2060. https://doi.org/10.1152/ajpheart.2001.280.5.H2053

Mamidi R, Gresham KS, Stelzer JE (2014) Length-dependent changes in contractile dynamics are blunted due to cardiac myosin binding protein-C ablation. Front Physiol 5:461. https://doi.org/10.3389/fphys.2014.00461

Marcucci L, Washio T, Yanagida T (2017) Titin-mediated thick filament activation, through a mechanosensing mechanism, introduces sarcomere-length dependencies in mathematical models of rat trabecula and whole ventricle. Sci Rep 7(1):5546. https://doi.org/10.1038/s41598-017-05999-2

Olah A, Nemeth BT, Matyas C, Horvath EM, Hidi L (2015) Cardiac effects of acure exhaustive exercise in a rat model. Int J Cariol 182(1):258–266. https://doi.org/10.1016/j.ijcard.2014.12.045

Pacher P, Nagayama T, Mukhopadhyay P, Batkai S, Kass DA (2008) Measurement of cardiac function using pressure-volume conductance catheter technique in mice and rats. Nat Protoc 3(9):1422–1434. https://doi.org/10.1038/nprot.2008.138

Pulcastro HC, Awinda PO, Methawasin M, Granzier H, Dong W, Tanner BC (2016) Increased titin compliance reduced length-dependent contraction and slowed cross-bridge kinetics in skinned myocardial strips from Rbm (20DeltaRRM) mice. Front Physiol 7:322. https://doi.org/10.3389/fphys.2016.00322

Rice JJ, Wang F, Bers DM, de Tombe PP (2008) Approximate model of cooperative activation and crossbridge cycling in cardiac muscle using ordinary differential equations. Biophys J 95(5):2368–2390. https://doi.org/10.1529/biophysj.107.119487

Schneider NS, Shimayoshi T, Amano A, Matsuda T (2006) Mechanism of the Frank–Starling law—a simulation study with a novel cardiac muscle contraction model that includes titin and troponin I. J Mol Cell Cardiol 41(3):522–536. https://doi.org/10.1016/j.yjmcc.2006.06.003

Shavik SM, Wall ST, Sundnes J, Burkhoff D, Lee LC (2017) Organ-level validation of a cross-bridge cycling descriptor in a left ventricular finite element model: effects of ventricular loading on myocardial strains. Physiol Rep. https://doi.org/10.14814/phy2.13392

Shoucri RM, Kohar R (2012) Criteria for study of heart failure derived from ESPVR. Conf Proc IEEE Eng Med Biol Soc 2012:5586–5589. https://doi.org/10.1109/EMBC.2012.6347260

Spottiswoode BS, Zhong X, Hess AT, Kramer CM, Meintjes EM, Mayosi BM, Epstein FH (2007) Tracking myocardial motion from cine DENSE images using spatiotemporal phase unwrapping and temporal fitting. IEEE Trans Med Imaging 26(1):15–30. https://doi.org/10.1109/TMI.2006.884215

Tajima Y, Makino K, Hanyuu T, Wakabayashi K, Amemiya Y (1994) X-ray evidence for the elongation of thin and thick filaments during isometric contraction of a molluscan smooth muscle. J Muscle Res Cell Motil 15(6):659–671

Trayanova NA, Rice JJ (2011) Cardiac electromechanical models: from cell to organ. Front Physiol 2:43. https://doi.org/10.3389/fphys.2011.00043

Xi C, Kassab GS, Lee LC (2019) Microstructure-based finite element model of left ventricle passive inflation. Acta Biomater 90:241–253. https://doi.org/10.1016/j.actbio.2019.04.016

Zhang X, Haynes P, Campbell KS, Wenk JF (2015) Numerical evaluation of myofiber orientation and transmural contractile strength on left ventricular function. J Biomech Eng 137(4):044502. https://doi.org/10.1115/1.4028990

Zhang X, Liu ZQ, Singh D, Wehner GJ, Powell DK, Campbell KS et al (2017) Regional quantification of myocardial mechanics in rat using 3D cine DENSE cardiovascular magnetic resonance. NMR Biomed. https://doi.org/10.1002/nbm.3733

Zhang X, Liu Z-Q, Campbell KS, Wenk JF (2018) Evaluation of a novel finite element model of active contraction in the heart. Front Physiol. https://doi.org/10.3389/fphys.2018.00425

Publisher's Note Springer Nature remains neutral with regard to jurisdictional claims in published maps and institutional affiliations.